Analysis of the Thermal Transfers in a VASM Crucible: Electron Beam Melting Experiment and Numerical Simulation

Jérémie Haag, Jonathan Martens, Bernard Dussoubs, Alain Jardy, Jean-Pierre Bellot

metals

MDPI

Article

Analysis of the Thermal Transfers in a VASM Crucible: Electron Beam Melting Experiment and Numerical Simulation

Jérémie Haag *, Jonathan Martens, Bernard Dussoubs, Alain Jardy and Jean-Pierre Bellot

Institut Jean Lamour (UMR 7198 Université de Lorraine/CNRS), Campus Artem, 2 allée André Guinier–BP 50840, Labex Damas, CEDEX 01, F-54011 Nancy, France; jonathan.martens@univ-lorraine.fr (J.M.); bernard.dussoubs@univ-lorraine.fr (B.D.); alain.jardy@univ-lorraine.fr (A.J.); jean-pierre.bellot@univ-lorraine.fr (J.-P.B.)

* Correspondence: jeremie.haag@univ-lorraine.fr; Tel.: +33-3-7274-2671

Received: 16 July 2020; Accepted: 19 August 2020; Published: 25 August 2020

Abstract: A description of the Vacuum Arc Skull Melting (VASM) process is presented showing its particularly complex features because of the mixing of porous raw materials with the dense remelted metal as well as the very high temperature and the highly transient nature of the process. This paper presents a 3D transient mathematical modelling of the heat transport with the aim of bringing a better understanding of the thermal behavior of the material into the crucible during a melting cycle. The model takes into account the heat input provided by the incoming metal thanks to an adaptive meshing, as well as the latent heat of solidification and the radiative heat transfers. An experimental validation of the model is presented where an electron beam heating source mimics the heat effect of the arc thanks to an excellent guidance of the beam over the melt surface. A comparison between the measured and calculated temperatures of a steel load is reported and reveals a satisfactory agreement. With very few adjustments, concerning mainly heat radiation at the top surface of metal into the crucible, the numerical model appears to be an efficient numerical tool to simulate the VASM process at the industrial scale.

Keywords: electron beam melting; vacuum arc skull melting; heat transfer modelling; metallic scraps; recycling

1. Introduction

One of the main objectives of the remelting processes of titanium alloys is to eliminate the two main types of exogenous inclusions: the low density inclusions (LDI), which include the hard-alpha (titanium enriched with interstitial elements such as nitrogen or/and oxygen), and the high density inclusions (HDI). These defects can cause premature fatigue failure of any mechanical part of plane, like critical rotating parts of aircraft engines [1,2], compromising its safety and structural integrity. Basically, melting technologies used in the titanium industry are vacuum arc remelting (VAR), plasma arc cold hearth melting (PACHM) [3], and electron beam cold hearth melting (EBCHM) [4,5]. Three successive VAR melts are requested to remove LDI and produce certified premium grade titanium alloys when only one is necessary after a prior cold hearth melting operation. In the latter case, LDI are removed more easily because of the long metal residence time within the horizontal refining hearth, enhancing the dissolution of solid inclusions. Furthermore, HDI are also trapped due to the density separation by settling in the mushy zone. Those technologies have been approved by customers for very demanding applications. However, the feedstock, which is composed of scrap and sponge, must be carefully sorted and cleaned up. In order to allow a large variety of scraps and reduce the cost, the vacuum arc skull melting (VASM) process was developed. It makes possible a

massive production of titanium alloys based on feedstock products with an outstanding flexibility regarding shapes and dimensions of metal pieces to be recycled.

1.1. Description of the VASM Process

The furnace of the VASM process is decomposed in two parts: (i) a crucible where the melting of a consumable electrode occurs and (ii) an ingot mold in which the liquid metal is poured. The first step has the particularity to create the skull which will be used as the electrode of the next melting cycle. This is accomplished by means of a parallelepiped crucible made from water-cooled copper panels bolted together [6]. At the beginning of each cycle, scrap of any type and size (called the initial load on Figure 1) is deposited in this crucible. Above the crucible, a consumable electrode is vertically hung from a ram which can be moved up and down. As stated above, this electrode is the skull from the previous cycle. The melting sequence begins when an electric arc is ignited between the lower tip of the electrode and the initial load in the crucible, causing melting of both. Liquid metal (originating mainly from the electrode) accumulates inside the crucible where it fills in a pool at the top before partly solidifying upon contact with the water-cooled panels. The metal within the crucible, constituted of the initial load, the solidified metal and the liquid pool is called the charge in this paper. When the mass of the liquid pool reaches an expected value, typically equal to the mass of the initial load, the electric arc is switched off. The crucible is then tilted and the liquid pool is poured into the ingot mold. After cooling under vacuum or an inert gas atmosphere, the furnace is unloaded: a new ingot is stripped from the mold, and a thick crust of solid metal, hereinafter called the skull, is stripped from the crucible.

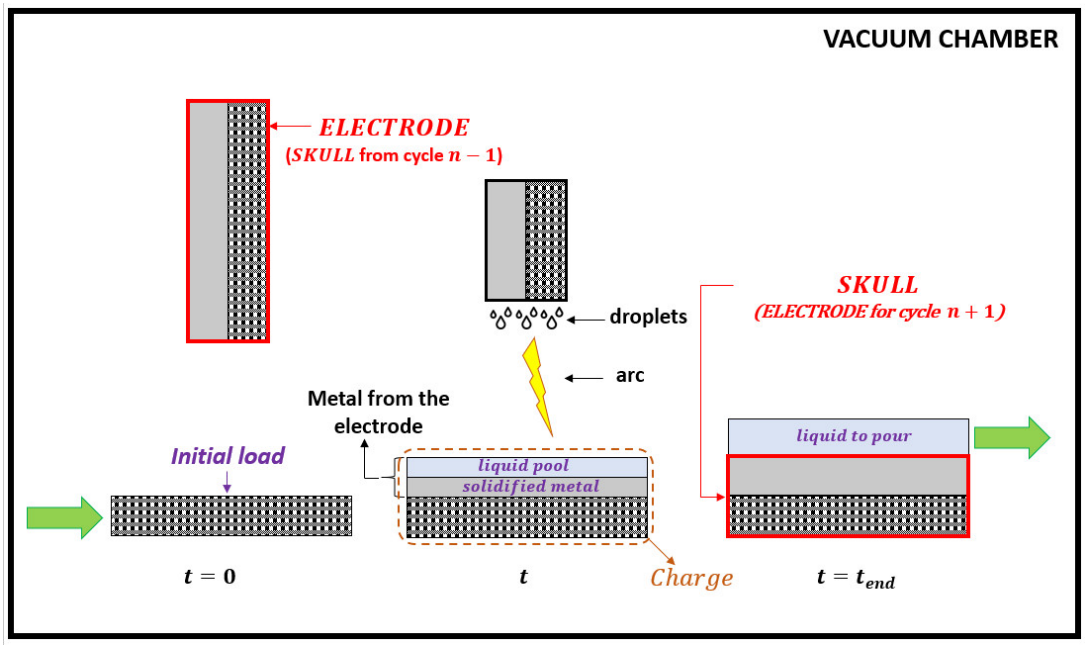

Figure 1. Schematics of the melting cycle of the VASM process.

The electric power is a main parameter of the process [7]. The arc must be powerful enough to maintain the molten metal in liquid state, counteracting against the radiative losses from the top surface as well as the losses to the cooled walls of the crucible. A carefully adapted electric power leads to a very limited over-heating of the melt. The heat balance evolves during the melting process, leading to an unsteady regime before the liquid pool volume remains constant.

Local intense heating of the crucible walls can lead to the formation of a crack, which might allow water from the cooling channel to penetrate the crucible and come into contact with the molten metal, hence an explosive reaction in the crucible. Ref [6] discussed the possible number of melting cycles before the next repair of the crucible, taking into account geometrical and structural criteria.

The literature on VASM process is particularly poor because of the relative novelty of the technology and of the confidentiality applied in a sensitive sector. Most of the literature states the main advantages and disadvantages of the VASM process among them the flexibility of the sources of raw material [8], the high degree of chemical homogeneity of the cast ingots [9], but with typical casting defects such as porous surface and shrinkage cavities. However, the main drawbacks can be overrun by remelting the produced ingot in a VAR furnace [9].

1.2. Objectives of the Present Study

In that context, it was decided to develop a transient 3D numerical model of the thermal transfers in the metallic load contained in the crucible, accounting for the continuous input of molten metal in order to bring a better understanding of the material behaviour during a melting cycle.

To compare the model results with experimental observation at a pilot scale, rather than using a VASM small-scale furnace, the use of an electron beam melting (EBM) device was preferred, as it allows a precisely controlled distribution of the energy input at the melt surface. The boundary conditions (see below) must obviously be derived to adapt to the specific apparatus used in the experiments.

It should also be noted that, in order to have a better control of the material homogeneity and make the experiments and temperature recordings easier, a packed bed of XC10 grade steel balls was used in this study in place of an actual load composed of Ti alloy scrap. Also, the feeding material is composed of the same steel. Therefore, the expected temperature of the liquid metal is of the order of 1550–1600 °C, slightly higher than the liquidus.

The outline of the present paper directly results from the above considerations. In Section 2, the experimental procedure is described in detail, with an emphasis on the insertion of a set of thermocouples within the initial load. The next section is devoted to the mathematical model itself. The boundary conditions correspond to the EBM device and will require an adaptation to VASM operation in a further step. Finally, the last section presents a comparison of the numerical results with the observations, as well as a simulation of the influence of an operating parameter, i.e., the total EB power.

2. Experiments

As stated in Section 1.2, the study involves achieving experiments using a suitable furnace in order to reproduce the behaviour of the molten metal during vacuum arc skull melting. A laboratory electron beam melting (EBM) furnace has been used for that purpose. After a first sub-section which details the experimental device, we will emphasize more particularly the operating conditions and the patterns which were effectively scanned by the electron beam.

2.1. Experimental Set-Up

The experiments have been conducted with a 100-kW laboratory EBM furnace (model: ALD–Lab100. ALD vacuum technologies, Hanau, Germany) as shown schematically in Figure 2. It includes a vacuum chamber (with a pressure lower than 10^{-3} mbar) and an EB gun with an accelerating voltage of 40 kV. A water-cooled copper crucible has been especially designed so as to mimic at the laboratory scale an industrial VASM crucible. The inside dimensions of the crucible are: $X_c \times Y_c \times Z_c = 125 \times 220 \times 150$ mm^3. Magnetic lenses enable a very accurate control of the beam motion, thereby of the heat power density according established pattern shapes and sizes. The automatic EB processes are operated by EB Scan and Control System (ESCOSYS®-ALD vacuum technologies, Hanau, Germany). All the variables involved in EBM process, such as beam pattern, beam power distribution and scanning frequency are governed by this operating system.

A drip melting experiment was performed to simulate the VASM process. Hence, steel balls ($d_p = 13$ mm) were initially loaded inside the crucible as a packed bed, leading to a porosity close to $\varepsilon = 0.36$. The height of the ball layer is $h_{IL} = 35$ mm. The steel ball layer mimics the scraps and raw materials in the VASM process and will be referenced as the initial load in this paper. A steel bar

(square section with $l_{bar} = 63$ mm) was positioned above and perpendicular to the crucible (see Figure 3a). During the melting, the steel bar was fed into the EB furnace at a constant speed by a bar pusher in order to keep the bar tip location constant, as shown in Figure 3b. Ten type K thermocouples (tc_1 to tc_{10}) were inserted within the steel ball layer at different heights (see Figure 3b). The locations of the thermocouples are also reported in the Table 1. During the melting process, the EB continuously melts the tip of the bar and steel droplets fall into the crucible where they may either immediately solidify or fill in a pool depending of the beam power. The steel alloy used for both the balls and the bar is a stainless steel whose properties will be reported in Section 3.3.

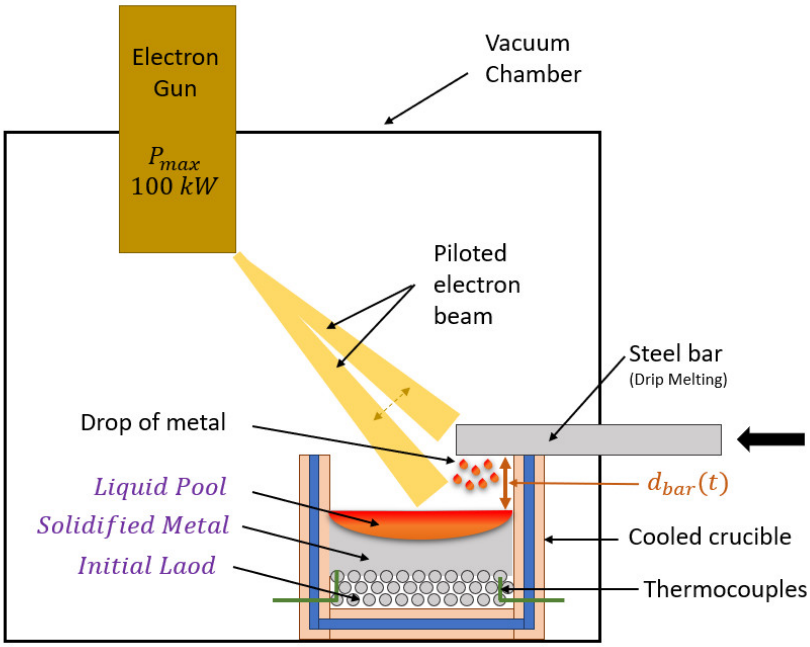

Figure 2. Schematics of the experimental set-up.

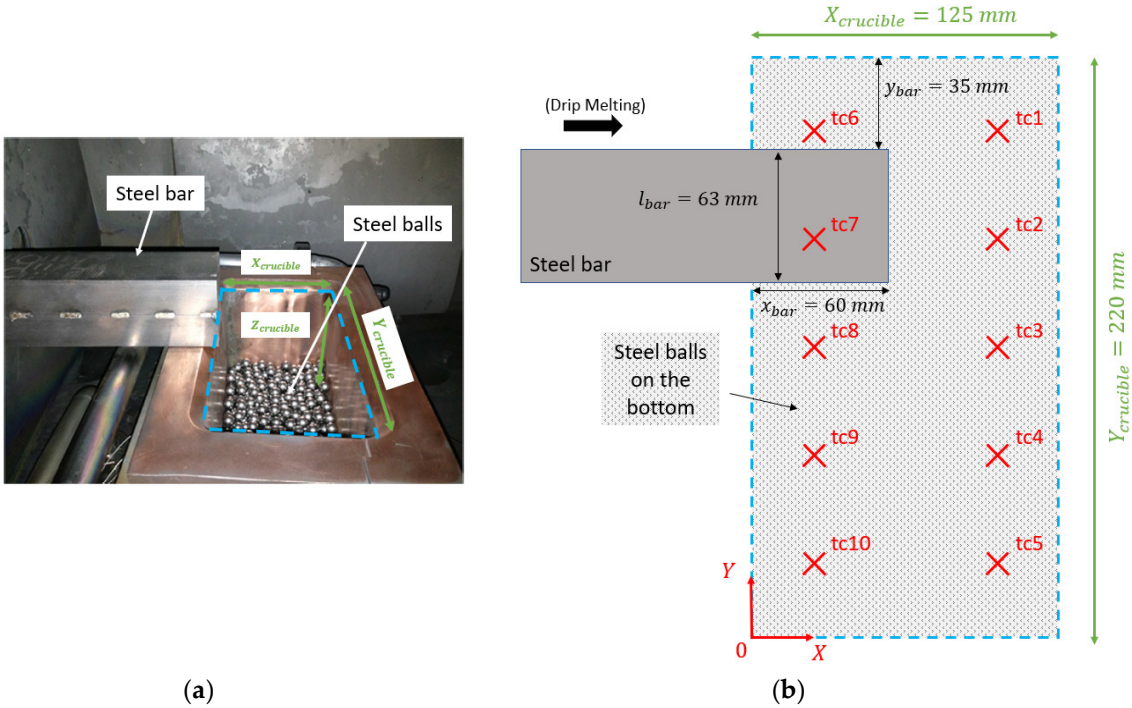

(**a**) (**b**)

Figure 3. Set-up of the water-cooled copper crucible. Picture of the crucible (**a**); top view (XY) of the crucible and locations of the thermocouples (**b**).

Table 1. Locations of the thermocouples.

Thermocouple	*X* (cm)	*Y* (cm)	*Z* (cm)
tc_1	10	16	2
tc_2	10	13.5	1
tc_3	11	11	3
tc_4	10.6	8.5	1
tc_5	10.2	6	2
tc_6	2.2	16	2
tc_7	2	13.5	1
tc_8	1.5	11	3
tc_9	1.7	8.5	1
tc_{10}	2.1	6	2

2.2. EB Operating Conditions

The intensity of the EB was linearly increased up to 0.5 A during the first 20 min and then was kept constant until the end of the melt, which means an electrical power equal to 20 kW as the voltage is kept constant $U = 40\ kV$. The melting rate was measured through the pushing speed of the bar feeder (13 mm/min once the steady state was reached) as $V_{fus} = 0.41\ \text{kg.min}^{-1}$. No experimental information is available concerning the moment t_{fus} when the actual melting started, so we estimated it at half of the transitory phase ($\Delta t_{init} = 20$ min) and assumed a linear variation of the melt rate from this moment until the steady state. All the operating conditions of the melting test are reported in Figure 4.

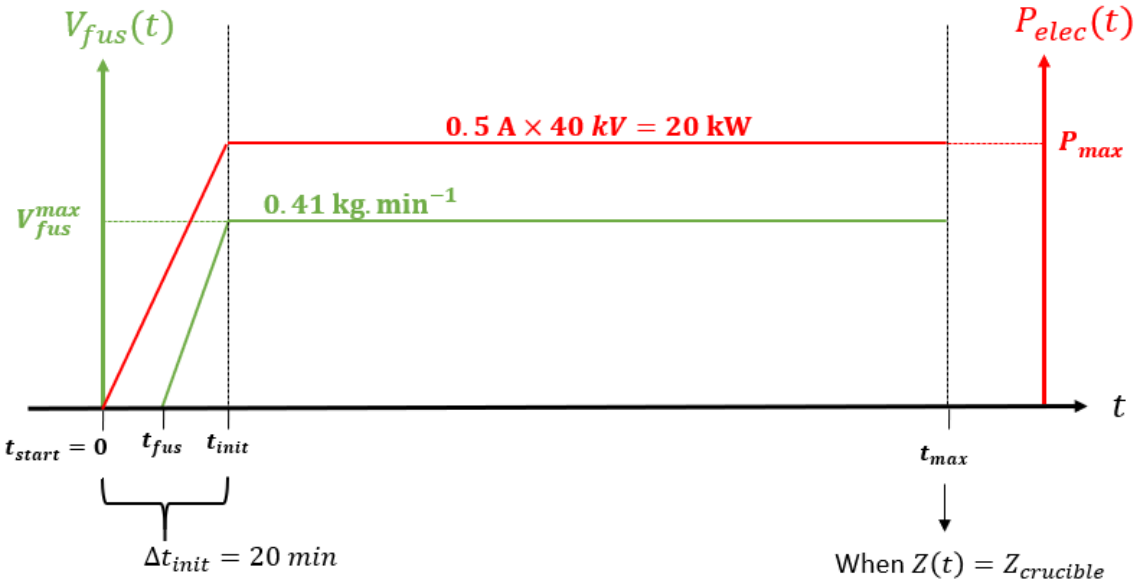

Figure 4. Experimental electrical power and melting rate versus time.

2.3. Electron Beam Pattern

During a full time period δt_{total}, the beam scanned three different patterns, as depicted in Figure 5: the "bar" pattern was applied for melting the bar tip, the "candle" pattern was devoted to ensure a total melting of the solid "candle" which may appear between the bar tip and the charge into the crucible, and the "pool" pattern was used to heat the surface of the metal in the crucible. The kinetic

energy of the beam is supposed to be converted to heat at the beam impingement with a yield η equal to 0.7 [10].

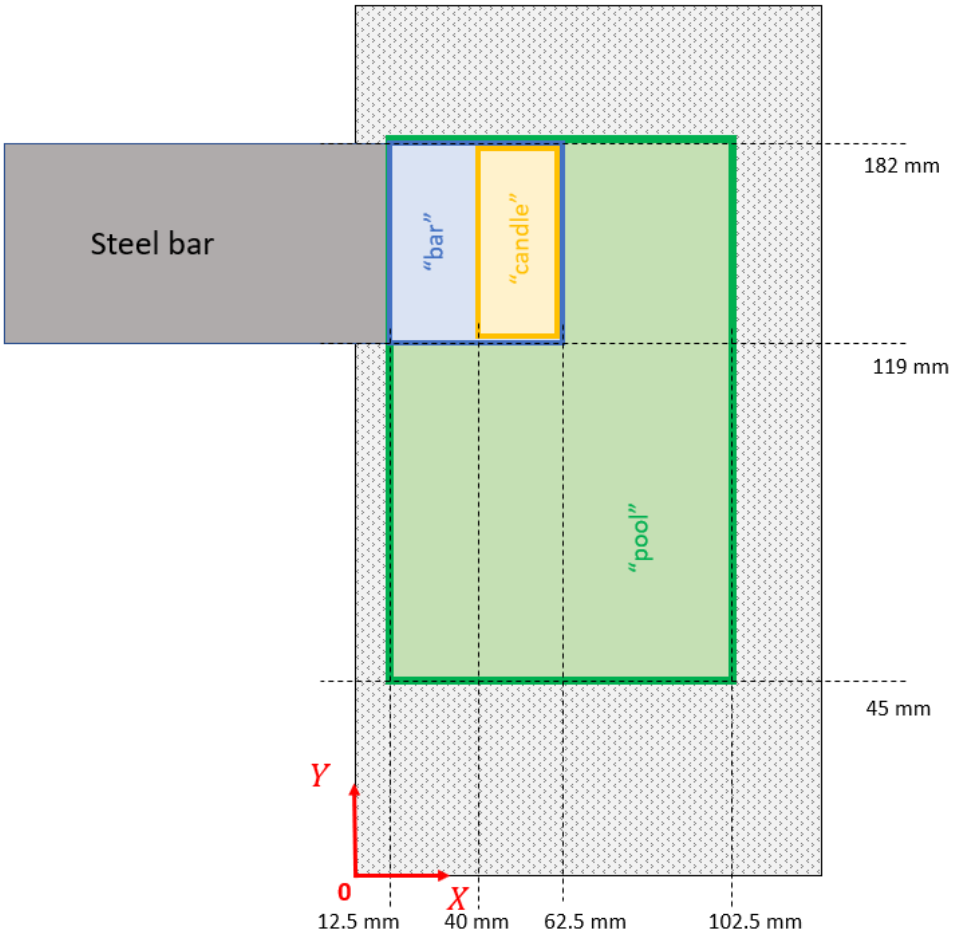

Figure 5. Electron beam patterns on the top of the charge.

For each pattern k, the exposure time δt_k defines the corresponding thermal power:

$$\delta t_{total} = \delta t_{pool} + \delta t_{bar} + \delta t_{candle} \quad (1)$$

Table 2 shows the values of the exposure times δt_k as well as the thermal powers and heat flux densities since we have:

$$P_{thermal,k} = \eta P_{elec} \frac{\delta t_k}{\delta t_{total}} \quad (2)$$

Table 2. Exposure time of the electron beam on each surface "pool", "bar" and "candle", and corresponding thermal power and flux density.

Surface k	Pool	Bar	Candle
Exposure time	$\delta t_{pool} = 125$ ms	$\delta t_{bar} = 100$ ms	$\delta t_{candle} = 100$ ms
Thermal power	5.38 kW	4.31 kW	4.31 kW
Area	12,330 mm^2	3150 mm^2	1417.5 mm^2
Thermal flux density	436.3 kW/m^2	1368.3 kW/m^2	3040.6 kW/m^2

3. Mathematical Modelling

A 3D mathematical model has been developed to simulate the transient heat transfer into the metal contained in the crucible, taken particularly into account as the heat input provided by the incoming metal thanks to an adaptive meshing, as well as the latent heat of solidification. The fluid flow in the liquid pool was not explicitly calculated but the convective heat transfer was modelled through the use of an effective conductivity. This is undoubtedly the main assumption of this model.

3.1. Heat Transport Equation

The general equation of heat transport is given by:

$$(1-\varepsilon)\rho\left(C_p + L_F\frac{\partial g_L}{\partial T}\right)\frac{\partial T}{\partial t} = \mathrm{div}\left(\lambda^*\vec{\nabla}T\right) + S_Z \tag{3}$$

where

- ρ: density $(\mathrm{kg.m^{-3}})$
- λ^*: effective thermal conductivity $(\mathrm{W.m^{-1}.K^{-1}})$
- T: temperature (K)
- S_Z: volumetric source term of heat $(\mathrm{W.m^{-3}})$
- C_p: specific heat at constant pression $(\mathrm{J.kg^{-1}.K^{-1}})$
- L_f: latent heat $(\mathrm{J.kg^{-1}})$
- g_L: liquid fraction $0 \le g_L \le 1$

The steel alloy in the crucible experiences solidification between the liquidus and the solidus temperatures. In the mushy zone, the liquid fraction g_L varies linearly from 0 to 1, which is a reasonable assumption because $T_{solidus}$ and $T_{liquidus}$ are quite close.

If $< T_{solidus}$:

$$g_L = 0 \tag{4}$$

If $T_{solidus} < T < T_{liquidus}$:

$$g_L = \frac{T - T_{solidus}}{T_{liquidus} - T_{solidus}} \tag{5}$$

If $> T_{liquidus}$:

$$g_L = 1 \tag{6}$$

The initial load is a porous media constituted of a packed bed of steel balls ($d_p = 13$ mm). Radiative fluxes between balls are taken into account by using a radiative thermal conductivity λ_{ray} [11].

$$\begin{cases} \lambda_{ray} = \dfrac{16}{3}\sigma d_{p,ray}T^3 \\ d_{p,ray} = \dfrac{2\varepsilon}{3(1-\varepsilon)}d_p \end{cases} \tag{7}$$

where ε is the porosity of the packed bed, supposed to remain constant ($\varepsilon = 0.36$).

In order to take into account the convective and turbulent heat transfer within the liquid phase, we artificially increased the thermal conductivity in the pool by introducing a multiplying factor k_λ. Such an important assumption has been used by several authors to roughly characterize the influence of turbulent convection in the liquid pool of ElectroSlag Refined (ESR) or Vacuum Arc Remelted (VAR) ingots [12–14]. Values for k_λ typically ranged between 2 and 6. Here, a value $k_\lambda = 5$ has been included in the model. With the aim of modelling all metal phases (liquid, mushy, solidified and initial load), an effective conductivity λ^* is introduced and calculated as:

$$\lambda^* = (1-\varepsilon)\left[1 + (k_\lambda - 1)g_L\right]\lambda + \lambda_{ray} \tag{8}$$

The parameters ε, g_L, and λ^* take different expressions as gathered in Table 3.

Table 3. Expressions of ε, g_L and λ^* depending on which phase is the metal.

Metal Phase	ε	g_L	λ^*
Liquid Pool	$\varepsilon = 0$	$g_L = 1$	$\lambda^* = k_\lambda \lambda$
Mushy zone	$\varepsilon = 0$	$0 \leq g_L \leq 1$	$\lambda^* = [1 + (k_\lambda - 1) g_L]\lambda$
Solidified metal	$\varepsilon = 0$	$g_L = 0$	$\lambda^* = \lambda$
Initial load	$\varepsilon \neq 0$	$g_L = 0$	$\lambda^* = (1 - \varepsilon)\lambda + \lambda_{ray}$

As it will be discussed, the numerical resolution of Equation (3) is performed using a finite volume technique, hence a structured mesh composed of hexahedral cells. The melting of the steel bar leads to a rise in the height of the charge with the processing time. This growth of the metal volume is accounted for by an adaptive mesh in the Oz direction. According to the melting rate V_{fus}, the height of the top layer of the mesh is increased at each time step and a new layer of cells is created when the top layer size becomes higher than a reference cell size. The steel droplets feeding the crucible are supposed to be at a temperature equal to:

$$T = T_{liquidus} + \Delta T_{sh} \quad (9)$$

where ΔT_{sh} is a superheat. The growth of the metal volume is taken into account by the source term S_Z in the heat transfer equation as we will see in next section.

3.2. Boundary Conditions

3.2.1. Top Surface

The boundary condition applied at the top surface of the domain is particularly complex since it is composed of three contributions as schematically illustrated Figure 6. These contributions are:

- φ_{elec}: the heat flux density provided by the electron beam
- φ_{drop}: the enthalpy flux density provided by the steel droplets
- φ_{rad}: the radiative net flux density emitted by the metal

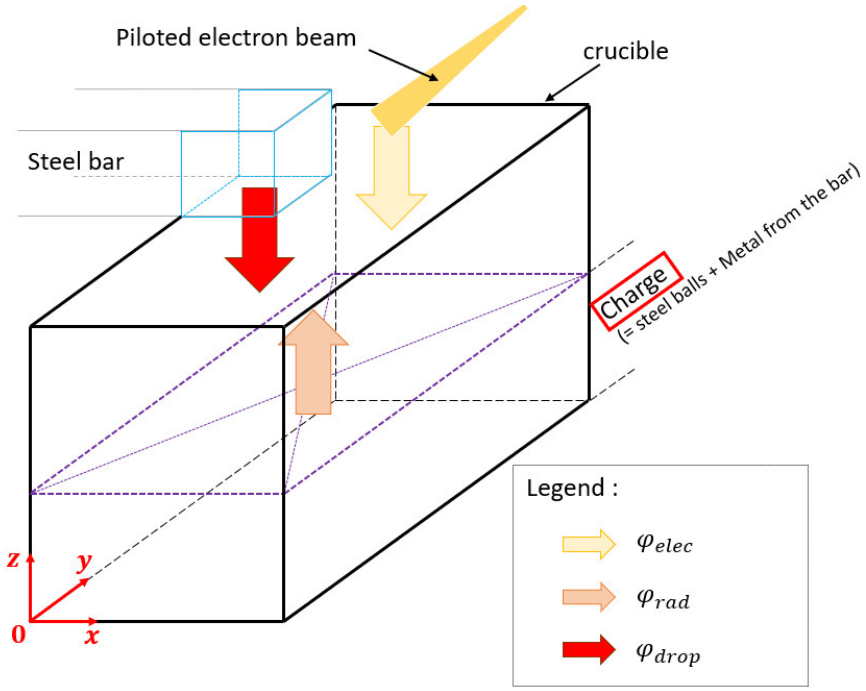

Figure 6. Schematic of the boundary conditions at the top of the crucible.

Electron Beam (EB) Heating

The beam scans only the central part of the crucible S^{pool} in order to avoid any beam-to-wall impingement. This pool surface is itself divided into four subzones as shown in Figure 7. Because of the shadowing influence of the steel bar, the subzone 3 is not heated by the beam. For the three remaining subzones, the heat density supplied by the EB is calculated as:

$$\varphi_{elec,k} = \frac{\eta P_{élec}}{S_k^{pool}} \times \frac{\delta t_{pool,k}}{\delta t_{total}} \quad (10)$$

where $\delta t_{pool,k}$ is the exposure time of the EB on S_k^{pool}. All the operating data are reported in the Table 4.

Table 4. Exposure time $\delta t_{pool,k}$ according to the subzone S_k^{pool}

Surface k	S_1^{pool}	S_2^{pool}	S_3^{pool}	S_4^{pool}
Area	3700 mm^2	2960 mm^2	3150 mm^2	2520 mm^2
% of "pool" area	30.0 %	24.0 %	25.6 %	20.4%
$\delta t_{pool,k}$	$0.3\delta t_{pool}$	$0.24\delta t_{pool}$	shadow	$0.204\delta t_{pool}$

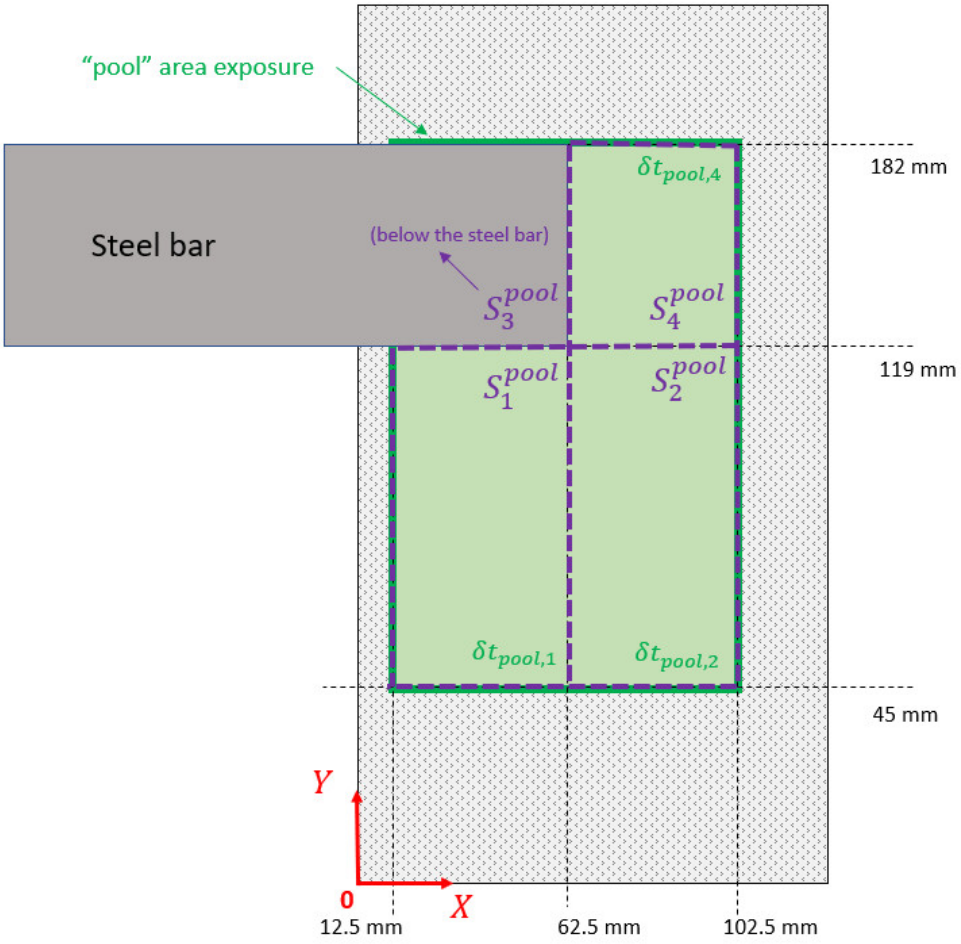

Figure 7. Subzones of the "pool" surface.

Enthalpy Flux Density Provided by the Droplets

In this section, we will make use of the following notations:

- h_0 is the specific enthalpy of the top layer at any time t_0:

$$h_0 = h_{ref} + (1-\varepsilon)(C_p T_0 + g_{L0} L_f) \quad (11)$$

- h_1 is the specific enthalpy of the top layer at any time $t_1 = t_0 + \Delta t$:

$$h_1 = h_{ref} + (1-\varepsilon)(C_p T_1 + g_{L1} L_f) \quad (12)$$

- h_{drop} is the specific enthalpy of the liquid drops falling during Δt:

$$h_{drop} = h_{ref} + C_p\left(T_{liq} + \Delta T_{sh}\right) + L_F \quad (13)$$

In the preceding, h_{ref} is the reference enthalpy at a standard state.

The enthalpy flux density provided by the droplets is given by:

$$\varphi_{drop} = \frac{V_{fus}.h_{drop}}{S_{crucible}} \quad (14)$$

As stated previously, this flux is incorporated in the model through an alike source term for all the cells in the top layer. At any time t_0, the volume of the top layer is equal to V_0. At $t_1 = t_0 + \Delta t$, this volume becomes:

$$V_1 = V_0 + V_{drop} \quad (15)$$

Between t_0 and t_1, if heat transfer within the crucible is neglected, the conservation of energy implies:

$$\rho h_0 V_0 + \rho h_{drop} V_{drop} = \rho h_1 V_1 \quad (16)$$

By combining Equations (15) and (16), we get:

$$\rho(h_1 - h_0)V_1 = \rho(h_{drop} - h_0)V_{drop} \quad (17)$$

$\rho(h_1 - h_0)V_1$ represents the rate of heat accumulation in the volume V_1 during Δt. The source term S_Z in Equation (3) must therefore be:

$$S_Z = \frac{\rho(h_{drop} - h_0)V_{drop}}{\Delta t \times V_1} \quad (18)$$

As the melting rate is $V_{fus} = \frac{\rho.V_{drop}}{\Delta t}$, we finally get:

$$S_Z = \frac{V_{fus}(h_{drop} - h_0)}{V_1} \quad (19)$$

Heat Loss by Radiation

The heat transfer by radiation between the steel bar, the top surface of the charge and the inner crucible wall plays an important role on the global heat balance. This is the reason why a precise calculation based on the determination of surface radiosities has been set up to get an accurate prediction of the net flux.

The space between the top of the charge and the tip of the steel bar is divided into 12 volumes having a rectangular parallelepiped shape (in purple in Figure 8), leading to a system of 52 surfaces. All solid surfaces are supposed to behave as grey bodies (i.e., their emissivity is independent on the temperature)

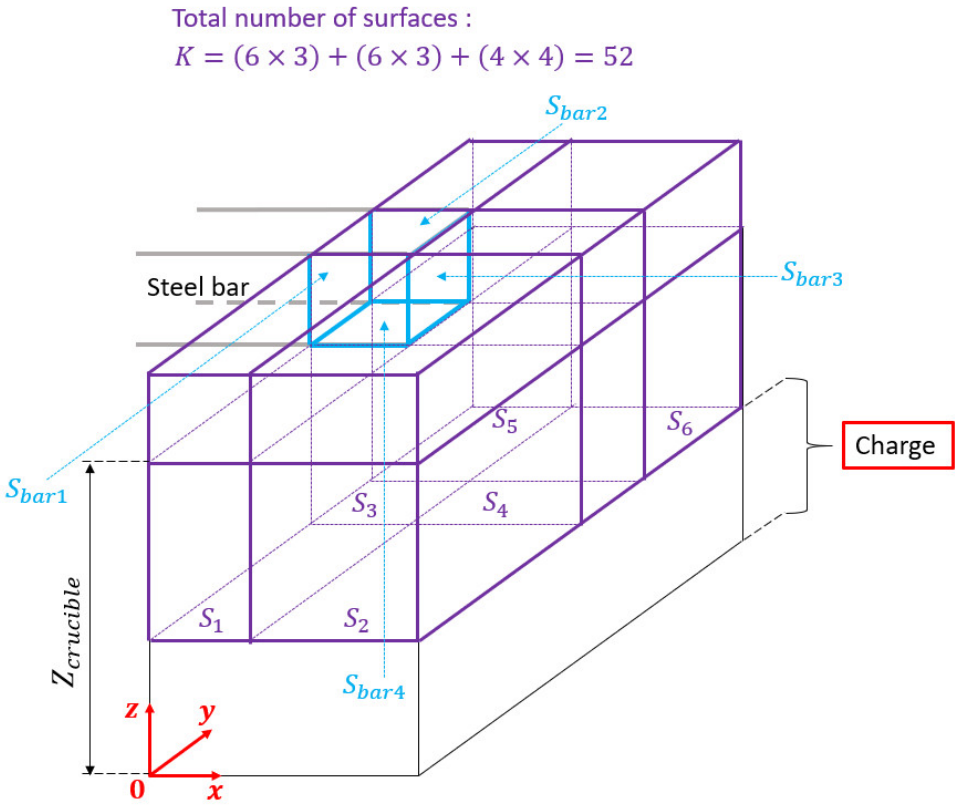

Figure 8. Meshing of the domain above the crucible top including the bar tip for radiative calculation purpose, the meshing of the charge is addressed in Section 3.3.

All the shape factors F_{jk} between surfaces j and k can be derived from geometrical considerations. The radiosity J_k emitted by each surface *k* is readily obtained by the inversion of the radiosity matrix [15]:

$$\begin{bmatrix} 1 & \cdots & -(1-\varepsilon_1)F_{1j} & \cdots & -(1-\varepsilon_1)F_{1K} \\ \vdots & \ddots & \vdots & & \vdots \\ -(1-\varepsilon_k)F_{k1} & \cdots & 1 & \cdots & -(1-\varepsilon_k)F_{kK} \\ \vdots & & \vdots & \ddots & \vdots \\ -(1-\varepsilon_K)F_{K1} & \cdots & -(1-\varepsilon_K)F_{Kj} & \cdots & 1 \end{bmatrix} \begin{bmatrix} J_1 \\ \vdots \\ J_k \\ \vdots \\ J_K \end{bmatrix} = \begin{bmatrix} \varepsilon_1\sigma T_1^4 \\ \vdots \\ \varepsilon_k\sigma T_k^4 \\ \vdots \\ \varepsilon_K\sigma T_K^4 \end{bmatrix} \quad (20)$$

where ε_k is the emissivity of surface *k*.

The net radiative flux density lost by the surface *k* is finally:

$$\varphi_{rad,k} = \frac{\varepsilon_k}{1-\varepsilon_k}(\sigma T_k^4 - J_k) \quad (21)$$

where σ is the Stefan–Boltzmann constant.

3.2.2. Crucibles Walls

The walls of the hearth are water-cooled copper panels. If a determination of the heat transfer coefficient for a casting mold is readily available [16,17], there is no accurate analysis in the literature dedicated to water-cooled refining hearths. A Fourier condition is applied to model the heat resistance between the solid steel, copper and the cooling water as:

$$\varphi_{cooling} = h_{eq}(T - T_{water}) \quad (22)$$

where

- h_{eq}: equivalent heat transfer coefficient $(\mathrm{W.m^2.K^{-1}})$
- T_{water}: temperature of the cooling water (K)

The water temperature is kept constant ($T_{water} = 20\,°\mathrm{C}$). The heat transfer coefficient should account for the solidification shrinkage and gap formation at the metal/crucible interface. In such conditions, the maximum value of h_{eq} can be estimated at $200\ \mathrm{W.m^2.K^{-1}}$ [18]. Furthermore, since the initial load is composed of steel balls, the contact between it and the crucible is very bad, leading to a weak heat transfer. Therefore, we have chosen an average value of the heat transfer coefficient equal to $50\ \mathrm{W.m^2.K^{-1}}$ at all the crucible walls.

3.3. Thermophysical Properties and Numerical Solution

The density and specific heat capacity of the stainless steel are kept constant with the temperature. According to the thermal properties reported in [19], the thermal conductivity linearly decreases from room temperature up to 800 °C. Hence, the conductivity halves over the temperature range as shown in Table 5, which gathers the set of data used in the simulation.

Table 5. Thermodynamic values of steel alloy, data from [19].

ρ	$7860\ \mathrm{kg.m^{-3}}$
L_f	$207\ \mathrm{kJ.kg^{-1}}$
C_p	$605\ \mathrm{J.kg^{-1}.K^{-1}}$
$T_{solidus}$	1534 °C
$T_{liquidus}$	1536 °C
ε_{steel}	0.3
$\varepsilon_{crucible}$	0.8
$\lambda(0\ °\mathrm{C})$	$65.2\ \mathrm{W.m^{-1}.K^{-1}}$
$\lambda(T \geq 800\ °\mathrm{C})$	$28.9\ \mathrm{W.m^{-1}.K^{-1}}$

The heat transfer Equation (3) is solved using a home-made finite volume code written in Fortran 90 using an implicit scheme with a time step equal to 1 s. The structured mesh is composed of $N_x \times N_y \times N_z(t)$ rectangular parallelepipedic cells. The total number of cells is equal to 256,000 at the start of the melting operation and reaches 768,000 cells at the end.

A global thermal balance was carried out to control the accuracy of the numerical procedure. All the components of this thermal balance are therefore calculated at each time step and the deviation of the balance is expressed as:

$$error\ (\%) = \left| \frac{P_{electron} + P_{drop} + P_{rad} + P_{cooling} - \dfrac{\Delta H_{acc}}{\Delta t}}{P_{electron} + P_{drop} + P_{rad} + P_{cooling}} \right| \times 100 \quad (23)$$

In the simulation reported below, this error remains lower than 2% at every moment.

4. Results

This chapter is divided into three sub-sections. The first examines the experimental results and the comparison with the numerical results is presented. Because the numerical simulation allows a deeper thermal analysis, a detailed investigation is reported in the second sub-section with a particular attention to the process heat balance. In order to guarantee the formation of a liquid pool at the top of the charge, a simulation with a higher EB power is eventually presented and analyzed.

4.1. Experimental Results and Comparison with the Numerical Simulation

The skull was easily removed from the copper crucible after cooling. Figure 9 reveals that the steel ball layer was not remelted and that the infiltration of liquid metal through the porous bed was hardly noticeable. Moreover, the top surface of the skull was far from flat and horizontal, and the

presence of a candle of solid metal reveals that the liquid steel heated at the tip of the bar was partly solidified before being in contact with the top of the charge.

Based on that observation, we can conclude that the remelted steel at the tip of the bar spread on the surface of the charge but also quickly solidified. According the EB thermal power condition prevailing in this experiment, the fill level was not uniform (as it is clearly observed in Figure 9b) which is not well modelled through the adaptive mesh.

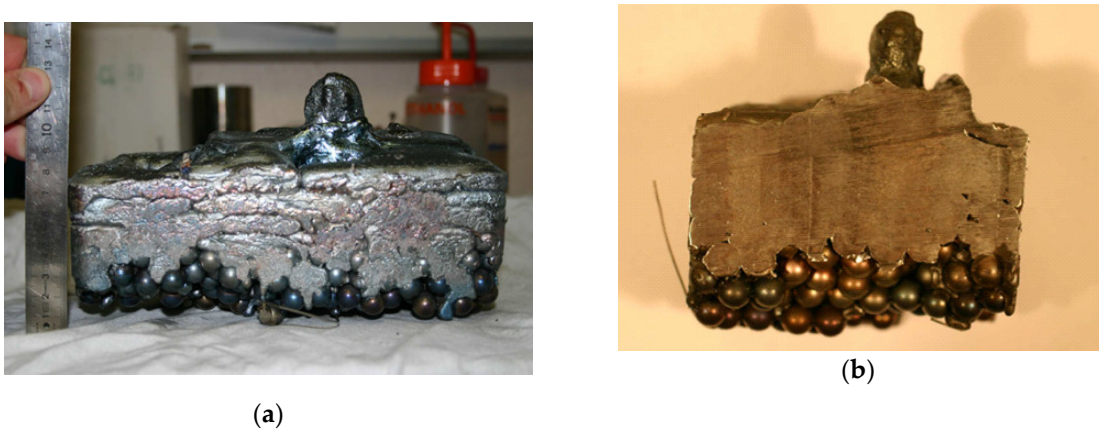

(**a**) (**b**)

Figure 9. Pictures of the skull after melting. (**a**) view from the side. (**b**) transverse cut.

The calculated height of the charge at the end of the remelting test (z = 8.25 cm) is in good agreement with the average value measured (see Figure 9a). This clearly indicates that, as assumed in the simulation, the liquid steel did not infiltrate the raw charge. Figure 10 confirms that the maximum temperature calculated by the numerical model remains lower than the liquidus temperature, i.e., the EB power applied at the top of the charge did not allow for the formation of an actual liquid pool.

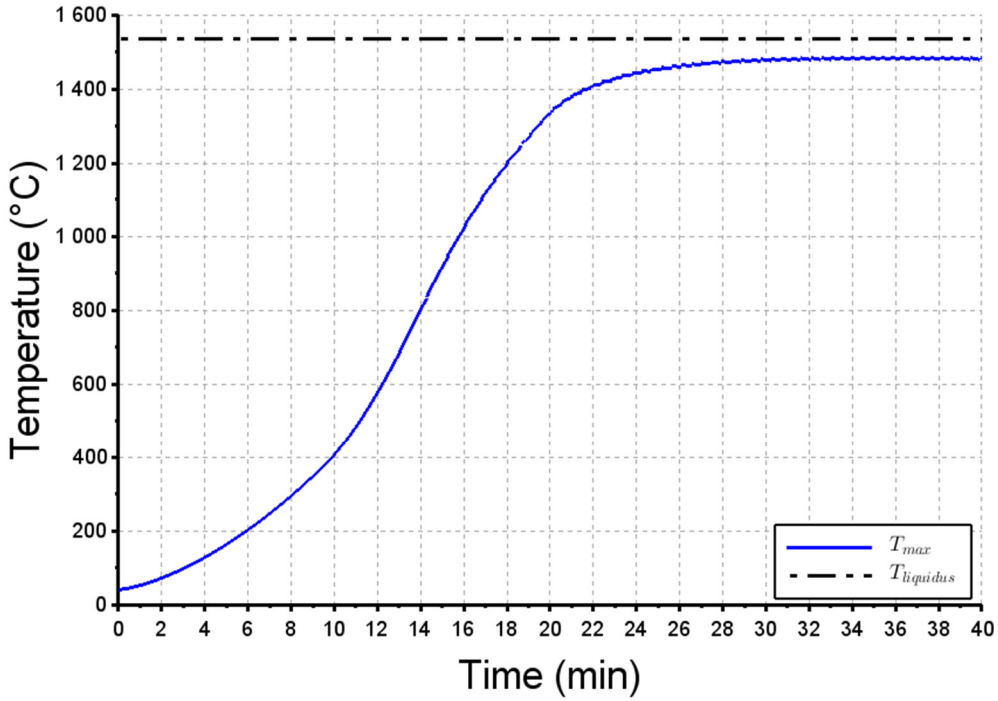

Figure 10. Maximum temperature calculated within the charge vs time. $T_{liquidus}$ = 1536 °C.

As stated previously, ten thermocouples have been installed within the steel ball layer (their location is shown in Figure 3). The actual and simulated thermograms are reported in Figures 11 and 12 respectively, for the 40 min of the melting trial. Again, all temperatures are much lower than the steel liquidus temperature, which implies that no liquid pool was formed during this melting operation. At the beginning of the experiment, the thermocouples tc_6 and tc_8 reached higher temperatures than the other ones. It could be explained by some rare infiltrations of metal within the initial bed of steel balls. Obviously because the infiltrations are not modelled, their thermal effect cannot be obviously observed in the numerical results. The other thermocouples display a similar dynamic behavior. We can observe a significant time-lag (around 10 min) required for the heat to diffuse from the top surface to the location of the thermocouples, followed by a temperature increase at a rate lying between 35 and 50 °C/min. Finally, the maximum temperature (800–1050 °C) was reached at t = 25 min. The calculated curves (Figure 12) match relatively well with these dynamics, showing a characteristic S-shape for a diffusive transfer. This is particularly true for the group of thermocouples (tc_3, tc_7, tc_9 and tc_{10}) where the dynamic behaviour (heating rate around 50 °C/min) and the maximum temperature (around 1000 °C) are well simulated. The agreement appears however weaker for another group of thermocouples (tc_1, tc_2, tc_4 and tc_5) since the time-lag and maximum temperatures do not match properly. This could be explained by the mediocre filling of the crucible with the incoming partly liquid steel.

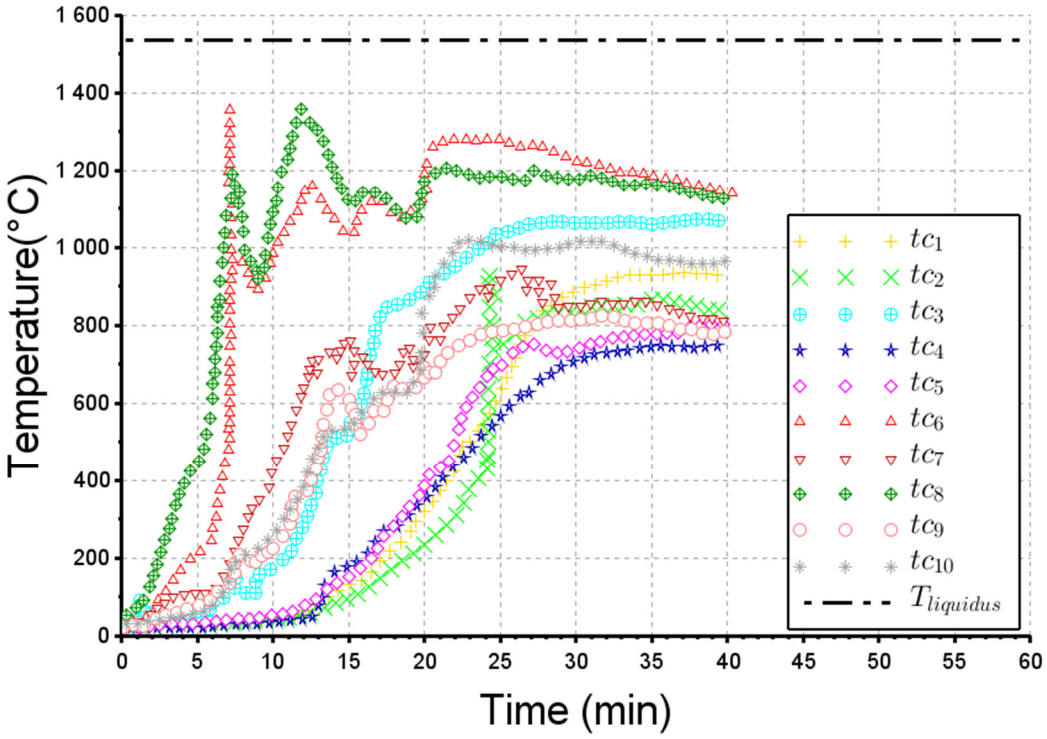

Figure 11. Actual thermograms from thermocouples tc_1 to tc_{10}. $T_{liquidus}$ = 1536 °C

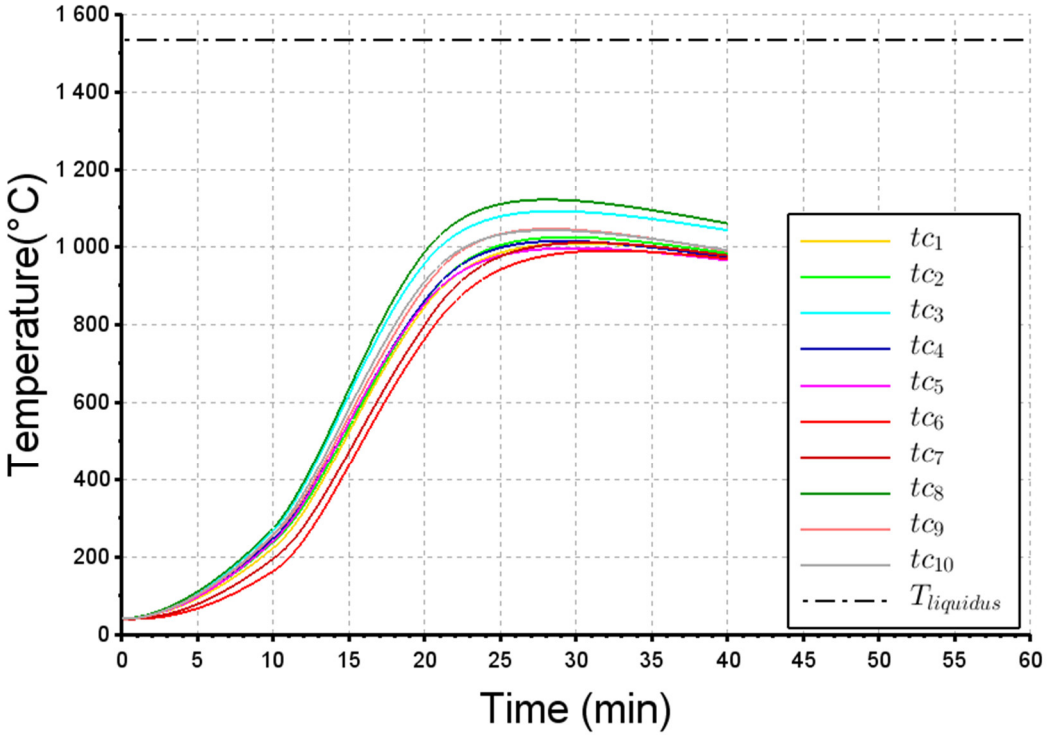

Figure 12. Computed temperature at the location of thermocouples tc_1 to tc_{10}. $T_{liquidus} = 1536$ °C

4.2. Analysis of the Numerical Results

The numerical simulation calculates the 3D temperature field at any time of the melting process as shown in Figure 13. An increase in the surface temperature with time is noticed, and the maximum surface temperature is located just below the edge of the steel bar (i.e., approximately above the thermocouple tc_8).

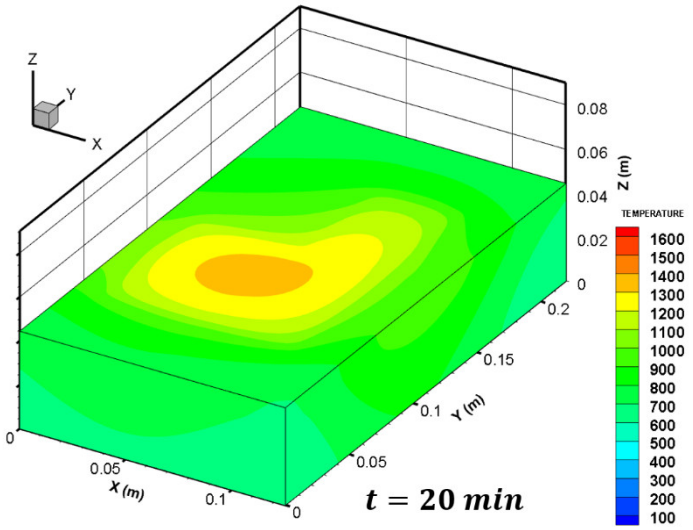

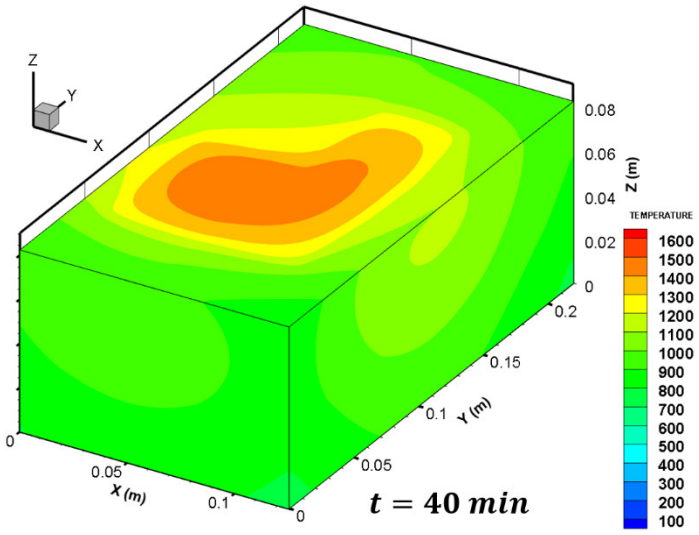

Figure 13. Three dimensional temperature field computed within the charge at $t = 20$ min and $t = 40$ min.

Associated with this thermal field, Figure 14 reports the global heat balance of the steel charge into the crucible, as assessed by the numerical simulation. The dotted green line and dotted purple line draw the thermal heat provided by the electron beam on the metal surface when the stationary melting rate is attained (4.01 kW) and on the bar (9.99 kW) respectively. Obviously, their sum is equal to the total beam thermal power:

$$P_{thermal}^{max} = \eta P_{elec} = 0.7 \times 20 = 14 \text{ kW} \quad (24)$$

The steel drops cast into the crucible brought an enthalpy flux (continuous red line) according to the equation:

$$P_{drop} = V_{fus} \times h_{drop} \quad (25)$$

When the stationary melting rate is attained this enthalpy flux reaches $P_{drop} = 9.06$ kW, so that the heat lost by radiation from the steel bar to the EB furnace corresponds to the difference between $P_{thermal,bar}^{max}$ and P_{drop}^{max}, i.e., $\Delta P_{loss} \cong 0.9$ kW.

The heat lost by radiation at the surface of the charge (blue curve) and to the cooling system (turquoise curve) evolves following the same trend and are approximately of the same order of magnitude, with a maximum value of 4 kW each. The thermal accumulation, which is not reported in the graph, compensates this heat balance, since the thermal capacity of the charge continuously rises with the processing time (growth of the mass of the steel block and increase in its temperature). Table 6 gathers the items of the heat balance near the end of the melting trial, and shows that more than 50% of the thermal EB power is lost through the cooling circuit of the crucible and by radiation at the top surface, while less than 40% remains in the growing charge. Finally, this lab-scale melting test consumed 0.81 kWh per kg of remelted steel (P_{elec}/V_{fus}) whereas the typical yield is around 1 kWh per kg for a single VAR [10].

Table 6. Heat thermal balance at t = 40 min.

Thermal power of the EB (kW)	14.0	100%
Thermal power lost by the steel bar (radiation) (kW)	0.9	6.4%
Thermal power lost by the charge (water cooling and radiation) (kW)	8.0	57.1%
Heating power of the charge (kW)	5.1	36.5%

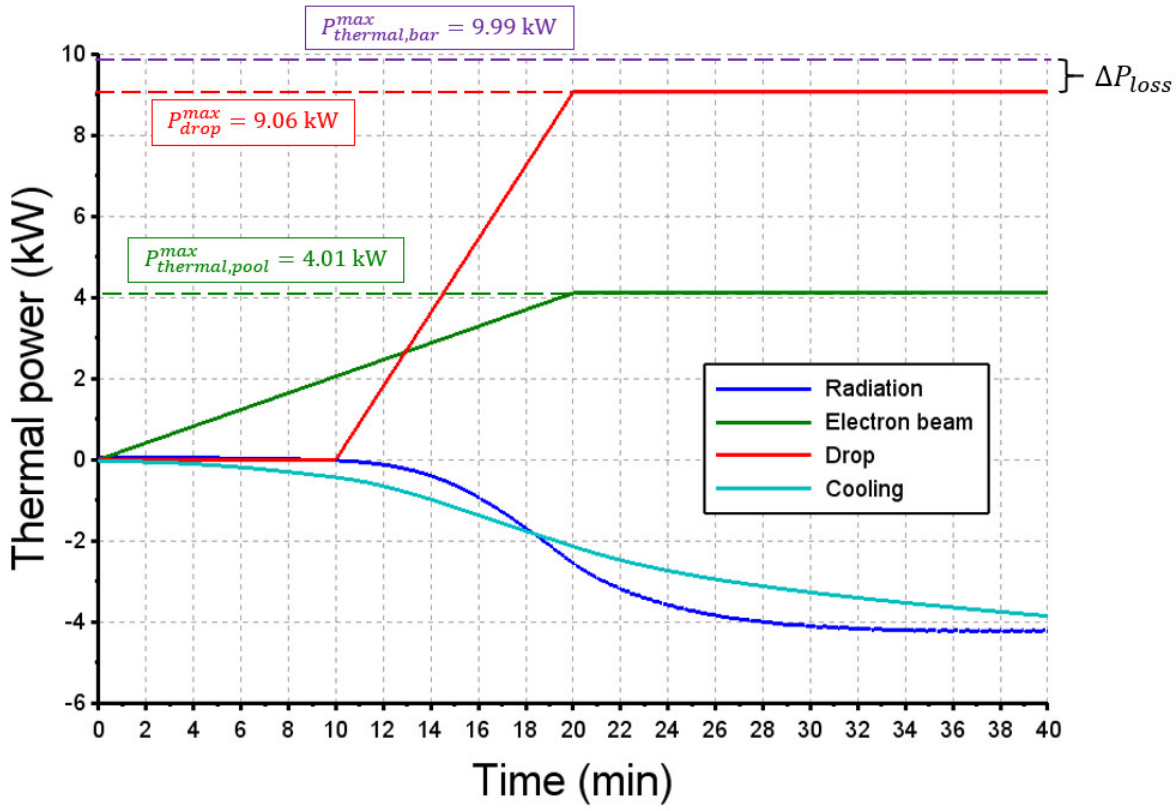

Figure 14. Assessment of the global heat balance of the charge with time. If positive, the heat power is received by the charge.

4.3. Simulation with a Higher EB Power

Since the obvious purpose of a process such as VASM is to actually remelt the raw material, a numerical simulation with a higher value for the EB power has been investigated in order to get an actual liquid pool.

The new operating conditions called thereafter as "power+" differ from the experimental operating conditions labelled as "reference" case only by the total EB power (see Table 7), all the other conditions and properties remaining the same.

Table 7. New operating conditions compared to the reference case.

Configuration	U(V)	I(A)	$P_{élec}$ (kW)	$P_{thermal,bar}$ (kW)	V^{max}_{fus}(kg. min^{-1})
"reference"	40,000	0.5	20	10	0.41
"power+"	40,000	0.9	36	18	0.74

The numerical results of this "power+" case simulation show that the initial load composed of steel balls is still not remelted since the top surface temperature of this ball bed remains below the liquidus temperature. The first drops of liquid steel (t = 10 min) solidify when contacting the steel balls but soon after the model predicts a liquid pool to be formed, as presented in Figure 15. The mass of the liquid bath increases slowly and continuously until reaching 1.5 kg, when the EB is switched off.

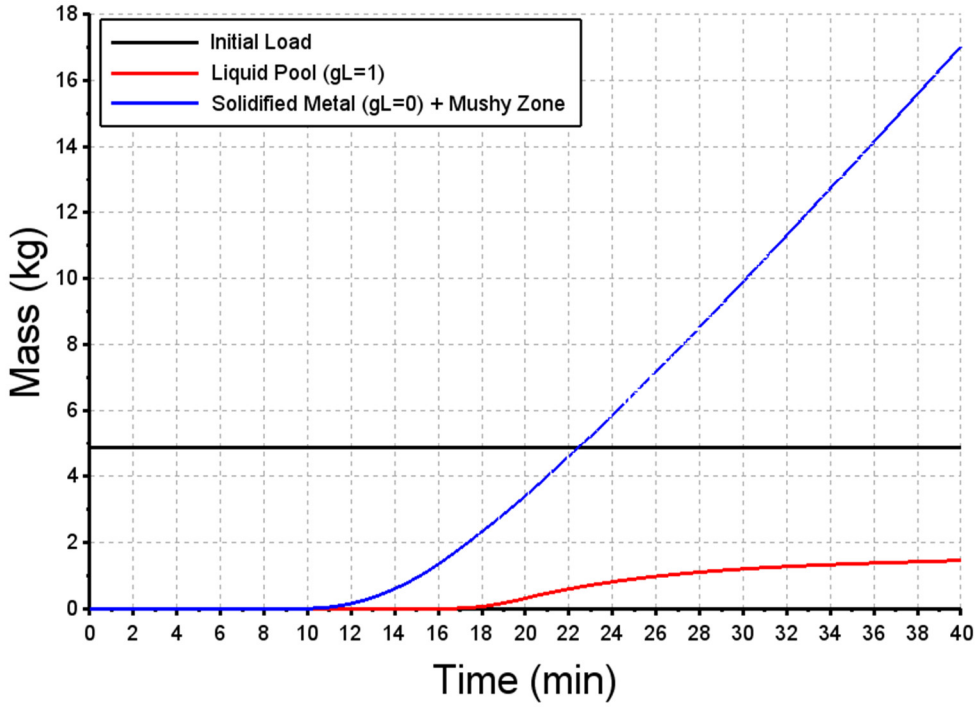

Figure 15. Predicted mass of the initial load (in black), of the liquid pool (in red) and of the solidified metal including the mushy zone (in blue) vs time. "power+" case.

At the end of the melting operation, the charge can be divided into three zones which are observed in the computed cross-section on Figure 16: the initial load made of steel balls, the solidified metal and eventually the liquid pool. The latter only involves only 6.4% of the total mass of the charge (see Table 8). This value is still far from the VASM industrial conditions where a final mass fraction of liquid pool of a third is expected (since the new consumable electrode is the skull of the previous melting cycle [8]).

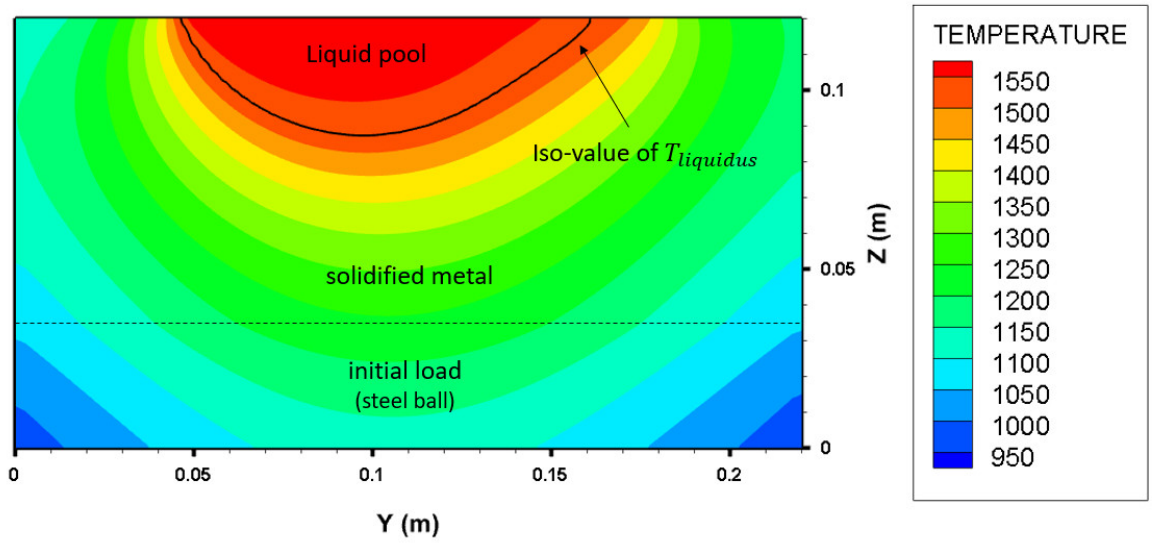

Figure 16. Computed cross-section of the crucible (X = 6.25 cm) at the end of melting (t = 40 min), showing the initial load, solidified steel and liquid pool predicted by the numerical model. "power+" case.

Table 8. Masses of the three parts of the charge at t = 40 min ("power+" case).

Total (kg)	23.3	100%
Mass of the initial load made of steel balls (kg)	4.8	20.6%
Mass of the solidified and mushy metal (kg)	17.0	73.0%
Mass of the liquid pool (kg)	1.5	6.4%

Such a difference is readily explained by the small dimensions of the lab-scale crucible, which enhance cooling at the crucible walls. Indeed, the ratio of the wall surface and the volume yields:

$$\frac{S_c}{V_c} = \frac{2}{X_c} + \frac{2}{Y_c} + \frac{1}{Z_c} \quad (26)$$

which decreases when scale-up the crucible size.

The corresponding thermal balance is reported in Table 9. Not surprisingly, comparison of Tables 6 and 9 indicates that an increase in the EB power results in an increase in the accumulation of enthalpy, correlated to the formation of the liquid pool.

Table 9. Heat thermal balance at t = 40 min (power+ case).

Thermal power of the EB (kW)	25.2	100%
Thermal power lost by the steel bar (radiation) (kW)	1.6	6.3%
Thermal power lost by the charge (water cooling and radiation) (kW)	13.2	52.4%
Heating power of the charge (kW)	10.4	41.3%

The ratio 41.3%/52.4% reported in Table 9 would then grow by increasing crucible size because of the aspect ratio mentioned earlier. The numerical modelling sounds a good approach for the assessment of the heat efficiency and liquid pool volume at the industrial scale.

5. Conclusions

In order to represent the thermal transfers within the liquid and solid parts of a metallic piece contained in a rectangular crucible continuously fed with liquid metal, a 3D numerical model has been set-up and applied to simulate a remelting test of stainless steel using a lab-scale electron beam melting (EBM) furnace. In addition to the evolution of the 3D temperature field with time, the model calculates the global heat balance experienced by the charge and the mass ratio of the three parts, i.e., the initial load, the solidified material, and the liquid pool.

Steel balls have been selected to mimic the porous initial load, which is industrially composed of scraps, sponge and master alloys during titanium vacuum arc skull melting (VASM). With very few adjustments concerning the boundary conditions, mainly the heat radiation at the top surface of the charge, the numerical model could enable us to simulate the VASM process at the industrial scale. However, it must be recalled that a "diffusion-only" heat transfer modelling can be considered as a limitation of this analysis and future work is needed to include turbulent convective transport in the liquid pool.

Concerning specifically the EB melting of stainless steel, the main results of this work are the following:

1. The initial porous layer underwent very little infiltration of liquid metal and was not remelted during the operation.
2. The EB power was not high enough to cause the apparition of a liquid pool at the top surface of the steel charge, and candle-shaped solidified steel was observed between the bar tip and top surface.
3. The numerical results match reasonably well with the postmortem observation of the steel block and with the temperatures measured by a set of thermocouples positioned within the initial load.

4. A further simulation with a higher EB power allows the prediction of a liquid pool. The simulation shows that the metal block can be divided into three parts at each time step, namely the bottom region made of initial porous layer, the intermediate region of solidified metal, and the liquid pool at the top.

Author Contributions: Conceptualization, J.-P.B. and A.J.; software, J.H. and B.D.; validation, J.H. and J.M.; resources, B.D. and J.M.; writing—original draft preparation, J.H.; writing—review and editing, J.H., J.-P.B., and A.J.; supervision, J.-P.B. and A.J. All authors have read and agreed to the published version of the manuscript.

Funding: This research received no external funding.

Acknowledgments: The authors gratefully acknowledge the financial and technical supports from Safran Group and wish to thank Benedicte Baqué, formerly postdoctoral intern at Institut Jean Lamour (IJL), for her contribution to EB experiments

Conflicts of Interest: The authors declare no conflict of interest.

References

1. Bellot, J.P.; Ablitzer, D.; Hess, E. Aluminum volatilization and inclusion removal in the electron beam cold hearth melting of Ti alloys. *Metall. Mater. Trans. B* **2000**, *31*, 845–854, doi:10.1007/s11663-000-0121-0.
2. Shamblen, C.E. *Technical Information Series Report R89AERB141*; General Electric Aircraft Engines: Cincinnati, OH, USA, 1989.
3. Yao, L.; Maijer, D.M.; Cockcroft, S.L.; Fiore, D.; Tripp, D.W. Quantification of heat transfer phenomena within the melt pool during the plasma arc re-melting of titanium alloys. *Int. J. Heat Mass Transf.* **2018**, *126*, 1123–1133, doi:10.1016/j.ijheatmasstransfer.2018.06.051.
4. Bellot, J.P.; Dussoubs, B.; Reiter, G.; Flinspach, J. A Comprehensive Numerical Modelling of Electron Beam Cold Hearth Refining and Ingot Consolidation of Ti Alloys. *Rare Met. Mater. Eng.* **2006**, *35*, 93–96.
5. Güther, V.; Allen, M.; Klose, J.; Clemens, H. Metallurgical processing of titanium aluminides on industrial scale. *Intermetallics* **2018**, *103*, 12–22, doi:10.1016/j.intermet.2018.09.006.
6. Goncharov, K.A. Stress-strain state and safe life of the crucible of a skull furnace under thermomechanical loading. *Metallurgist* **2011**, *54*, 852–858, doi:10.1007/s11015-011-9384-8.
7. Ricci, M.; Santin, G. Skull melting plant-a "stand-alone" facility for melting of titanium and zirconium. *Heat Process.* **2009**, *7*, 323–327.
8. Costanzi, M. *The Skull Melting Furnace and the Recycling of Titanium and Zirconium Scrap*; Materiaux: Nantes, France, 2010.
9. Fischer, D.; Guglielmi, F. *Skull Melting, an Alternative Melting Process for the Production of Ti 6Al-4V Aerospace Plates*; Japan Institute of Metals: Kyoto, Japan, 2007; p. 4.
10. Schiller, S.; Heisig, U.; Panzer, S. *Electron Beam Technology*; Wiley: New York, NY, USA, 1982; ISBN 978-0-471-06056-7.
11. Zhou, X.; Torero, J.L.; Goudeau, J.C.; Bregeon, B. On the Propagation of a Reaction Front through a Porous Fuel in the Presence of an Opposed Forced Flow: Application to Mixtures Characteristic of Municipal Waste. Combust. *Sci. Technol.* **1995**, *110–111*, 123–146, doi:10.1080/00102209508951919.
12. Ballantyne, A.S. Heat Flow in Consumable Electrode Remelted Ingots. Ph.D. Dissertation, University of British Columbia, Vancouver, VN, Canada, 1978.
13. Choudhary, M.K. A Study of Heat Transfer and Fluid Flow in the Electroslag Refining Process. Ph.D. Dissertation, MIT, Cambridge, MA, USA, 1980.
14. Jardy, A. Modélisation des Procédés de Refusion à Électrode Consommable—Application à l'Inconel 718. Ph.D. Dissertation, INPL, Nancy, France, 1984.
15. Sacadura, J.F. *Transferts Thermiques Initiation et Approfondissement*; Lavoisier Tech & Doc: Paris, France, 2015; ISBN 978-2-7430-1993-8.
16. Zhao, X.; Reilly, C.; Yao, L.; Maijer, D.M.; Cockcroft, S.L.; Zhu, J. A three-dimensional steady state thermal fluid model of jumbo ingot casting during electron beam re-melting of Ti–6Al–4V. *Appl. Math. Model.* **2014**, *38*, 3607–3623, doi:10.1016/j.apm.2013.11.063.
17. Shuster, R.E.; Cockcroft, S.L.; Maijer, D.M.; Yao, L.; Tripp, D.W.; Fiore, D. A three-dimensional transient thermal-fluid flow-compositional study of ingot casting during electron beam remelting of Ti–6Al–4V. *Appl. Math. Model.* **2016**, *40*, 9095–9117, doi:10.1016/j.apm.2016.05.037.

18. Kobryn, P.A.; Semiatin, S.L. Determination of interface heat-transfer coefficients for permanent-mold casting of Ti-6Al-4V. *Metall. Mater. Trans. B* **2001**, *32*, 685–695, doi:10.1007/s11663-001-0123-6.
19. ASM International Handbook Committee. *ASM Handbook, Volume 1: Properties and Selection: Irons, Steels, and High-Performance Alloys*; ASM International: Cleveland, OH, USA, 1990; Volume 1; ISBN 978-0-87170-377-4.